Article

Poly Meta-Aminophenol (PmAP) as a Solid-State Electron Mediator in the Z-Scheme, Ag_3PO_4/$CoFe_2O_4$ Heterojunction: Mineralization of Highly Concentrated Bisphenol-A and Reactive Dyes Water Pollutants

Chirasmayee Mohanty, Alaka Samal,* Ajaya K. Behera, and Nigamananda Das*

Read Online

ACCESS | 📊 Metrics & More | 📖 Article Recommendations | 🆂🅸 Supporting Information

ABSTRACT: This study demonstrated the effectiveness of poly meta-aminophenol (PmAP) as a solid electron mediator in the Z-scheme photocatalytic system for organic pollutants (viz. bisphenol-A and reactive dyes) mineralization and also illustrated how PmAP transported the photogenerated electrons from an O_2-emitting photocatalyst (Ag_3PO_4) to a H_2-emitting photocatalyst ($CoFe_2O_4$) enabling enhanced photocatalytic activity under visible light irradiation. The PmAP/Ag_3PO_4−$CoFe_2O_4$ (PAC-10), was prepared by a two-step process and characterized by various analytical methods to assess the impact of PmAP on optical, photocatalytic, and electrochemical characteristics of the $CoFe_2O_4$ (CFO)/Ag_3PO_4 composite. The morphological investigation revealed that the PmAP sheet was nicely decorated with evenly distributed Ag_3PO_4 and $CoFe_2O_4$ particles. The M−S plot and impedance analyses were used to assess the electrochemical capabilities of the catalyst. Z-scheme charge transfer pathways were well supported by the radical trapping experiment and HRTEM analysis of Pt photodeposited PAC-10 photocatalysts during the photoreaction. Because of its magnetic nature and ease of synthesis, the PAC-10 offers an easily recyclable Z-scheme photocatalytic system that has the potential for purifying wastewater with high concentrations (up to 100 mg/L) of organic pollutants within 30 min of visible light exposition.
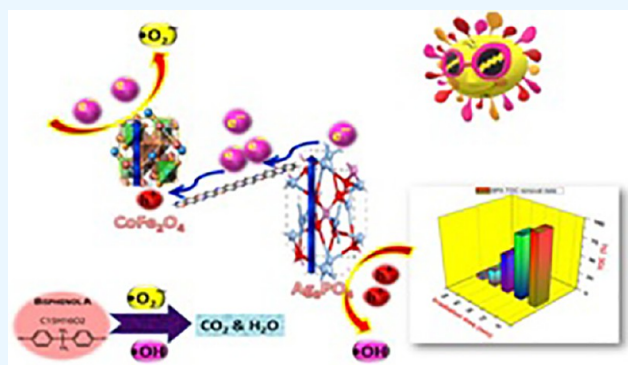
INTRODUCTION

Most durable plastics that people routinely use contain a chemical compound known as bisphenol A (BPA). Higher BPA dosages have been associated with adverse consequences like infertility, some cancer kinds, and various other health issues.[1] Prenatal BPA exposure may have a long-lasting effect on the development of cancer in specific organs. Hormone-related malignancies could also arise as a result of regular exposure to high-content BPA.[1] Consumers are routinely exposed to this extensively used chemical through food, beverages, and water sources, as minute levels may seep out or leach out from the food packaging.[2,3] Organic dyes are another class of commonly occurring pollutants in wastewater due to their excessive use in a wide range of products. To get rid of these kinds of organic contaminants from water bodies, photocatalysis has been proven to be a simple, effective, and inexpensive process that uses photocatalysts and light sources only.[4−6] Development of visible light active multicomponent heterostructure catalytic system with superior performance over single component catalysts like TiO_2, ZnO, Ag_3PO_4, CdS, WO_3, etc. in terms of efficacy, stability, and facile regeneration is desirable.[7−9] Very often, these heterostructure systems have

cumbersome synthetic procedures and lack adequate activity for the removal of these organic contaminants at higher concentrations.

It has already been established that Z-scheme photocatalytic systems have better charge carrier separation and more efficiency as compared to other conventional heterostructures due to the perfect band alignments and higher redox potential ability of the system. For a perfect Z-scheme heterostructure, two photocatalysts viz. one H_2-producing (having negative E_{CB}) and the other O_2 (having positive E_{CB}) were commonly employed and often with the assistance of an electron shuttle.[10] Tada et al. recommended the all-solid-state Z-scheme photocatalyst[11] for the first time to widen the practical scope of the liquid-phase Z-scheme process. In these systems, a solid such as noble metal Au, Ag, or conductive carbonaceous
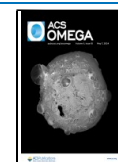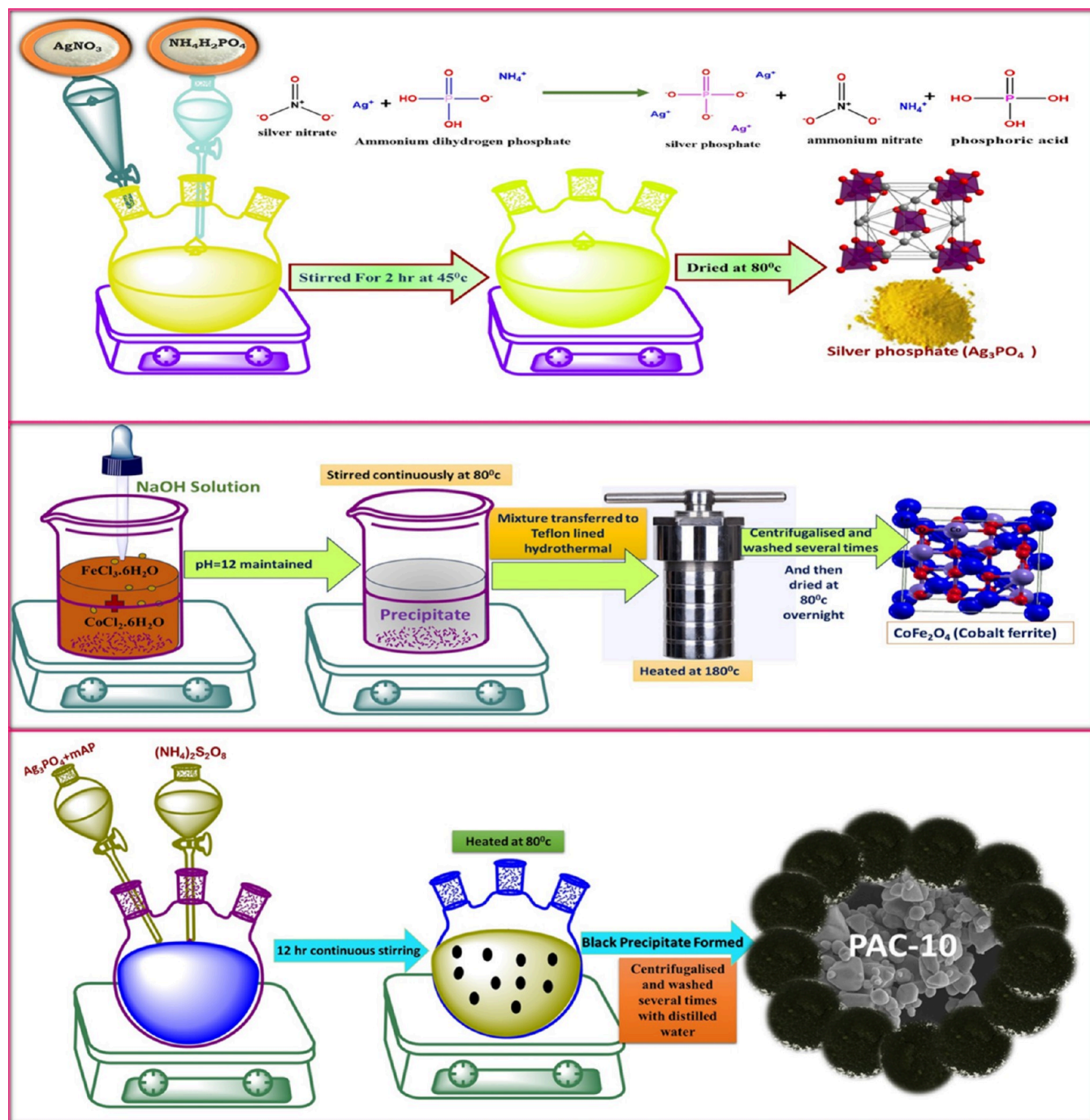
Scheme 1. Schematic Representation of Synthesis Methods for Ag$_3$PO$_4$, CFO, and PAC-10 Catalysts

material substitutes for the original liquid electron shuttle.[12,13] Amal and co-workers[14] used the reduced graphene oxide as a solid electron mediator for water splitting under visible light.

Poly meta-aminophenol (PmAP), a derivative of polyaniline (PANI) with two potentially active functional groups (−NH$_2$ and −OH) possesses good adsorption capacity in comparison to PANI with relatively good conductivity, electrochemical recurrence, and stability in water-based solutions.[12,15] Many studies have been published on the use of polyaniline in photocatalysis,[16−21] but there is no report available to date on the use of PmAP in a photocatalytic system as far as we are aware. In this work, the PmAP was introduced in a Z-scheme catalytic system with H$_2$ evolving (CoFe$_2$O$_4$) and O$_2$ evolving

(Ag$_3$PO$_4$) cocatalysts. CoFe$_2$O$_4$ (CFO), being a magnetic iron-based semiconductor oxide with high chemical stability, low toxicity, and high coercivity, has garnered significant interest in the field of photocatalysis.[20] Many review articles have been published focusing on its augmented activity in wastewater treatment and H$_2$ production from water.[20−22] The potential of CoFe$_2$O$_4$ in H$_2$ evolution reactions via water splitting, superconductivity, photocatalysis, and lithium-ion batteries has been explored.[23,24] Use of the CoFe$_2$O$_4$, neat or in association with a cocatalyst/noble metals for H$_2$ production has been reported by several workers.[25−27] In contrast, Ag$_3$PO$_4$ is a superior visible light active catalyst that has 90% quantum efficiency in oxygen evolution reactions.[28−30] It has dozens of
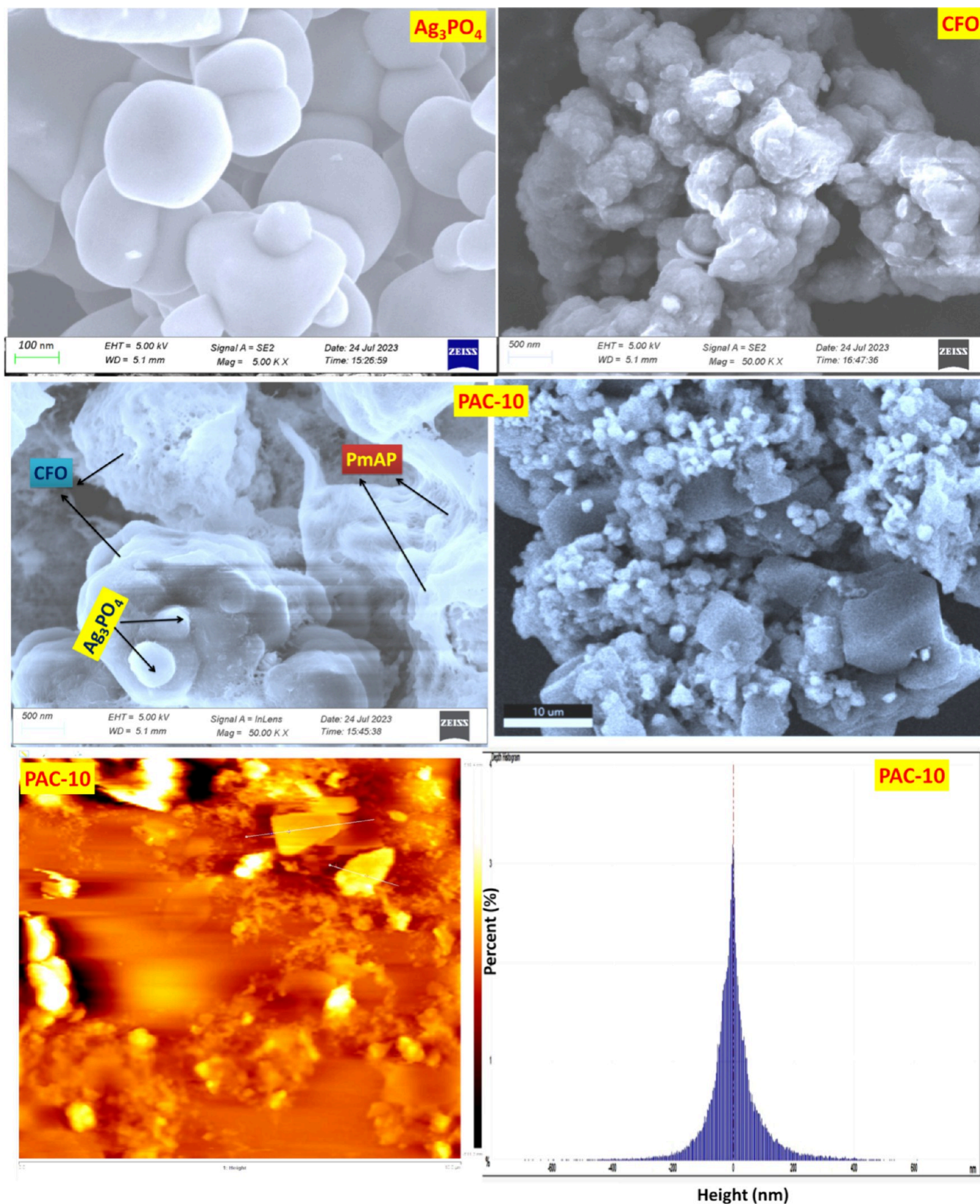
Figure 1. SEM image of the Ag₃PO₄, CFO, and PAC-10 Z-scheme heterojunction system. AFM images depicting 2D topography (left) and their height distribution in nanometers (right) for the PAC-10 composite.

times more potential than the commercial TiO_2 and $BiVO_4$ catalysts in terms of dye degradation reactions.[28−30] The combination of both CFO and Ag_3PO_4 showed exceptional photoactivity in dye removal applications but failed with highly concentrated dye solutions and recyclability points.[31−33] Many authors designed the Z-scheme catalyst based on $Ag_3PO_4/$

$CoFe_2O_4$ with and without a mediator or electron shuttle.[31−35] Herein for the first time, PmAP was used in this heterojunction as a mediator to yield a Z-scheme heterojunction with augmented activity for remediation of highly concentrated aquatic pollutants within minutes under visible light illumination. Establishing a dynamic equilibrium among the mediator's electron-donating and electron-accepting capabilities is the difficult part of creating a solid-state electron mediator as it keeps the mediator mostly unaltered during the process.[14,50] An ongoing electron flow between the source and target photocatalysts is also dependent upon the photocatalyst mediator photocatalyst contact interface.

Keeping these points in mind, the PmAP was designed and employed as the solid-state electron mediator that has excellent electrical conductivity, stable chemical structure under ambient circumstances, and π-conjugate long-chain polymeric structure with an easy synthetic procedure. Furthermore, the desire for clean water with a simple effective recovery process of the used photocatalyst after the reaction led to the selection of the $PmAP/Ag_3PO_4/CoFe_2O_4$ magnetic composite system.

■ EXPERIMENTAL SECTION

Synthesis of PmAP. PmAP was synthesized via a chemical polymerization method[36,37] utilizing ammonium persulfate as the oxidant. To initiate the synthesis, 0.03 mol of m-amino phenol was combined with 50 mL of aqueous hydrochloric acid (1.8 M) in a double-necked round-bottom flask. Subsequently, a solution containing 0.045 mol of ammonium persulfate, dissolved in 25 mL of water, was added dropwise to the monomer solution over the duration of 1.0 h under constant stirring. Following the completion of the addition, the entire content in the flask was subjected to heating at 80 °C with continuous stirring for a period of 10−12 h. This thermal treatment resulted in the formation of a deep brown precipitate of PmAP. The precipitate, separated through filtration, was subjected to washing with 4 M hydrochloric acid several times to eliminate any residual unreacted monomer or oligomers and then with distilled water until the filtrate achieved neutrality. Finally, the purified PmAP was dried at 70 ± 2 °C in a vacuum oven for 12 h.

Synthesis of Cobalt Ferrite. Cobalt ferrite nanoparticles were successfully synthesized by a hydrothermal method. A precursor solution was prepared by dissolving $FeCl_3·6H_2O$ (13.51 g, 2 mol) and $CoCl_2·6H_2O$ (5.94 g, 1 mol) separately in 30 mL of distilled water. The two solutions were then combined under continuous stirring, and glycerol (0.078 M) was slowly introduced. The pH of the resulting solution was carefully maintained at ~12.0 through the controlled addition of dilute sodium hydroxide. Following the formation of a brown precipitate, the entire mixture was further stirred for 30 min before being transferred to a Teflon-lined autoclave. The autoclave was sealed and subjected to hydrothermal treatment in an oven set at 180 °C for a duration of 6 h. After the mixture cooled, the black precipitate was separated through centrifugation, subjected to multiple washes with distilled water to eliminate chloride ions, and subsequently dried at 80 °C overnight. The resulting dried materials were securely stored in airtight containers for future utilization.

Synthesis of Silver Phosphate. For the synthesis of silver phosphate, solutions of $AgNO_3$ (0.3 M, 1.27 g) and $(NH_4)_2H_2PO_4$ (0.45 M, 1.29 g) were prepared in separate beakers. The controlled addition of $(NH_4)_2H_2PO_4$ solution into the solution of $AgNO_3$ under constant stirring at a

temperature of 45 °C over a period of 4 h resulted in the formation of a discernible yellow precipitate. The separated silver phosphate was thoroughly rinsed with a solution of ethanol/water (65/35 v/v %) to eliminate impurities. The washed product was finally dried overnight at 80 °C.

Construction of Visible-Light-Driven $PmAP/Ag_3PO_4−CoFe_2O_4$ Z-Scheme Heterojunction (PAC-10) Systems. In the pursuit of developing efficient hybrid composites for dye mineralization applications, a two-step process was employed to prepare the $PmAP/Ag_3PO_4−CoFe_2O_4$ Z-scheme heterojunction system. Initially, stochiometric amounts (10 wt %) of the prepared Ag_3PO_4 and $CoFe_2O_4$ (80 wt %) were ultrasonically homogenized in 20 mL of distilled water for 30 min. Simultaneously, PmAP (10 wt %) was synthesized via the chemical polymerization method as described above to which the suspension of $CoFe_2O_4$ and Ag_3PO_4 was added. The whole reaction mixture was heated at 80 °C with continuous stirring for 10−12 h, resulting in the formation of a solid $PmAP/Ag_3PO_4−CoFe_2O_4$ Z-scheme heterojunction (PAC-10). The ensuing solid composite material was vacuum filtrated, thoroughly washed with ethanol/water (65/35 v/v %), and dried at 70 °C overnight.

The schematic representations of all of the synthesis processes are shown in Scheme 1.

■ RESULTS AND DISCUSSION

Morphological Analysis. The as-prepared photocatalyst materials were examined by using scanning electron microscopy (SEM) to investigate their morphological structure and interfacial features. The morphological observations of Ag_3PO_4, CFO, and PAC-10 heterojunctions are depicted in Figure 1. The analysis reveals that pure Ag_3PO_4 has practically spherical shapes with diameters in the 100−400 nm range. In the case of pristine CFO, agglomerated clusters with unclear morphology and the size of the particles are observed. Interestingly, the SEM image of PAC-10 heterojunction shows that the big CFO particles (1−2 μm) and the small Ag_3PO_4 particles (300−400 nm) are effectively combined indicating an excellent connection among the CFO and Ag_3PO_4 components owing to the presence of conducting PmAP layers. This observation also indicates the successful synthesis of the Z-scheme PAC-10 heterojunction system through an easy hydrothermal process that helped the growth of the structures on the continuous layers of the PmAP. However, the intergranular aggregation of nanoparticles obscures the clear morphological view in the PAC-10 nanocomposite through the SEM analysis.[34,35] This agglomeration might be due to the presence of interfacial grain reactivity owing to the magneto statics interaction and the exchange dipole moment of particles having wide surface active sites in the PAC-10 heterojunction system.[38−40] The PAC-10 AFM top view analysis also confirms the similar rough topology and morphology with agglomerated particles, as depicted in Figure 1. It shows (2-D) AFM images as well as the height variations and roughness of the sample. As can be seen in the figure, for PAC-10, the size distribution is quite narrow. The representative AFM image and particle size distribution histograms for PAC-10 with a mean height value of 594.00 nm are shown in Figure 1.

To get more insight into the interfacial connection between the particles of CFO, Ag_3PO_4 on the PmAP layers, TEM analysis was employed for the PAC-10 photocatalytic system. The close integration of the CFO and Ag_3PO_4 particles with
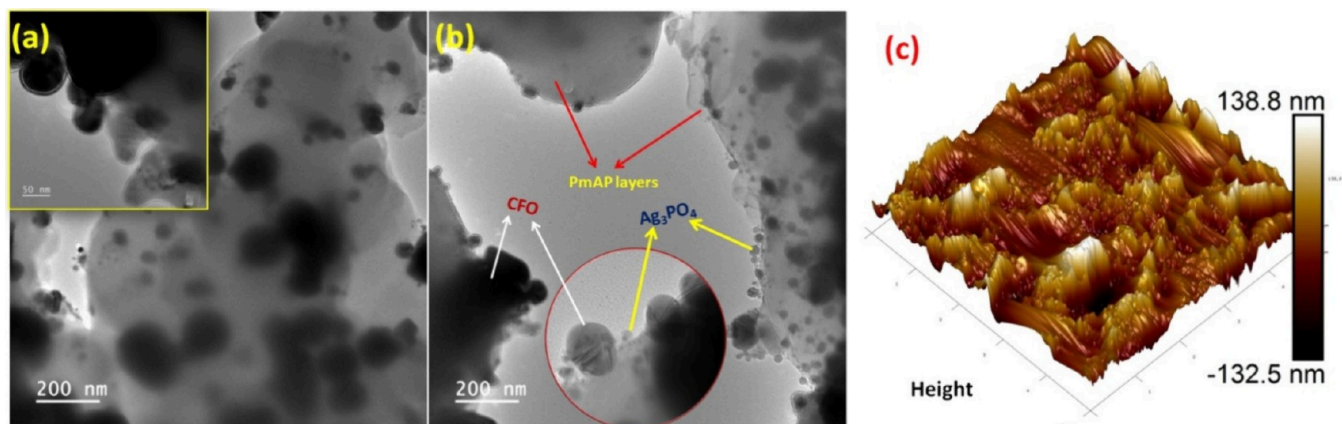
Figure 2. TEM analysis of the PAC-10 composite catalyst (a, b). (c) 3-D AFM images height map of the PAC-10 composite catalyst.
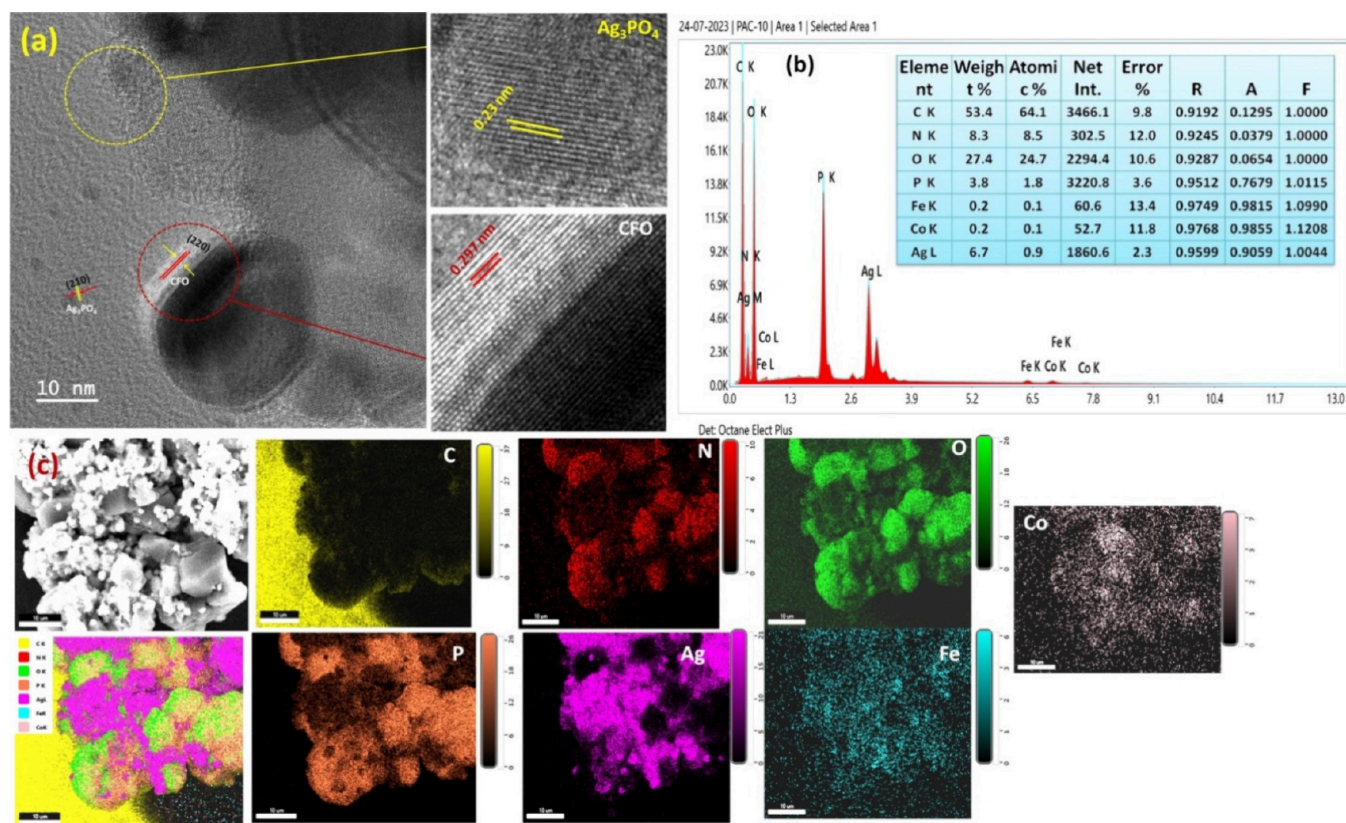

Figure 3. (a) HRTEM analysis, (b) EDS spectrum, and (c) elemental mapping of the PAC-10 nanocomposite.

the PmAP sheet is evident from Figure 2a,b. The obtained images demonstrated the fact that the PmAP structure consists of several layers exposing more edges. It also supports the well-decorated ornamentation of PmAP polymer layers with the large CFO and tiny Ag_3PO_4 particles. Unlike SEM, in TEM analysis, the individual semiconductor catalysts are noted very clearly. Particle aggregation in the SEM data made it impossible to compute the precise particle sizes of individual catalysts. TEM also shows that the CFO is in contact with the PmAP layers that have sizes within 100−300 nm. While the Ag_3PO_4 nanoparticles are found to be 10−30 nm in size and evenly spread over the polymeric layers. In the AFM of PAC-10 (Figure 2c), the observed 3-D surface topography is also uneven/rough. This implies that the sample consists of many sheetlike structures that create a layered object along with the

Ag_3PO_4−$CoFe_2O_4$ nanocomposites, which are attached on the layered surface evenly.

Additional evidence of the existence of the PmAP surface tailored with CFO and Ag_3PO_4 particles is provided by the high-resolution TEM (HRTEM) images of the PAC-10 heterojunction system presented in Figure 3. Using HRTEM images, the confirmation of synthesis and internal structure of the $CoFe_2O_4$ and Ag_3PO_4 nanoparticles on the PmAP layers were examined and are shown in Figure 3a. Based on HRTEM images (Figure 3a), the interplanar spacings of the cubic spinel crystals of $CoFe_2O_4$ and Ag_3PO_4 were calculated. The layer spacing of 0.297 nm can be ascribed to the (220) crystal plane of CFO, while that of 0.23 nm to the (210) crystal plane of Ag_3PO_4[40] further confirms the successful design of the PAC-10 composite. The corresponding chemical constituents of PAC-
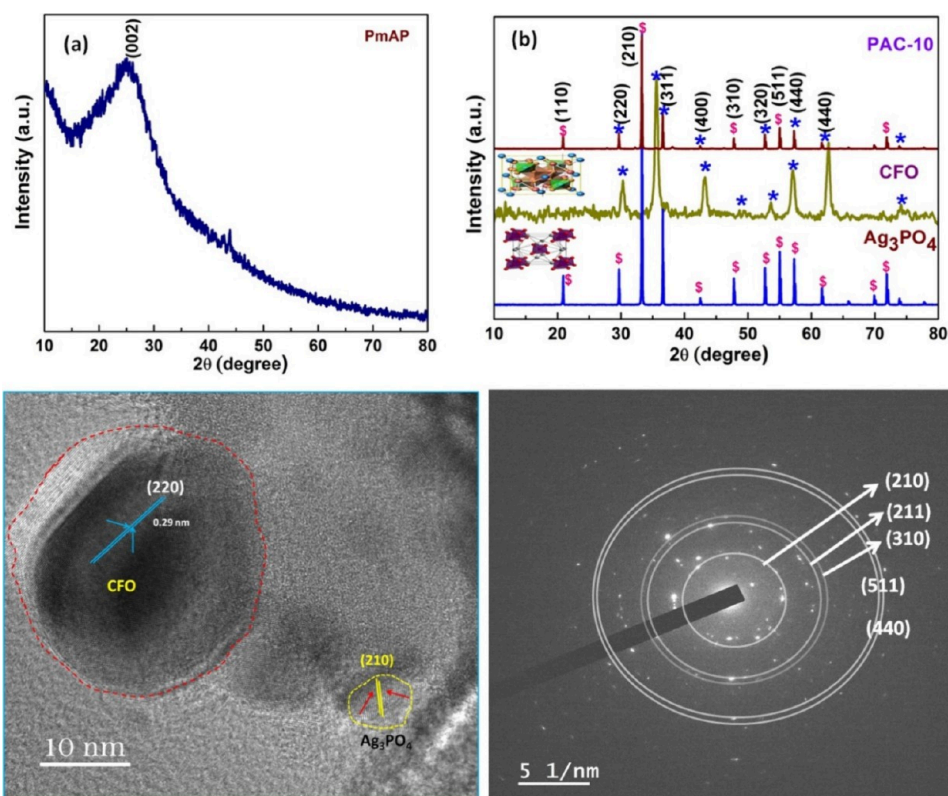
Figure 4. (a) XRD of PmAP, (b) CFO, Ag₃PO₄, and PAC-10 catalysts, with corresponding HRTEM analysis and SAED pattern of PAC-10 depicting consistent results with XRD analysis.
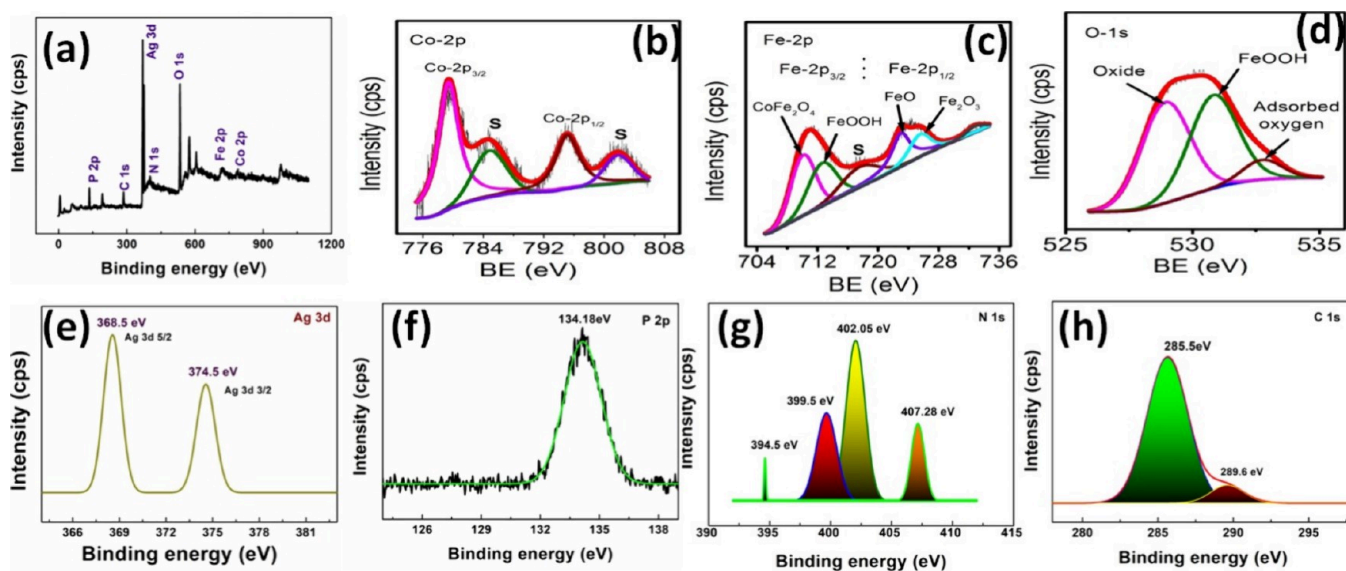

Figure 5. (a) Full XPS survey of PmAP/Ag₃PO₄/CoFe₂O₄ (PAC-10) composite; (b) Co 2p, (c) Fe 2p (d) O 1s, (e) Ag 3d, (f) P 2p, (g) N 1s, and (h) C 1s XPS scan spectra of PAC-10 composite.

10 heterojunction were verified by EDS analysis, which shows the presence of Ag, P, O, Co, Fe, C, and N elements in the PAC-10 (Figure 3b). To make sure the elements were distributed uniformly, EDS elemental mapping was taken at several places in the specimen which shows uniform distributions of constituent elements throughout the nanocomposite. Uniform distributions of constituent elements over the entire morphology without the presence of any unintended

elements corroborating the purity of the synthesized PAC-10 composites.

Structural Analysis. The results obtained from the HRTEM analysis are found to be consistent with the XRD data analysis, which can be verified in Figure 4. In the powder XRD pattern of pristine PmAP, the characteristic peak at $2\theta = 25.2°$ due to the (002) plane ascertains the formation of PmAP (Figure 4a). The XRD pattern of pristine CFO nanoparticles shows the existence of six clear distinctive peaks at $2\theta = 30°$,
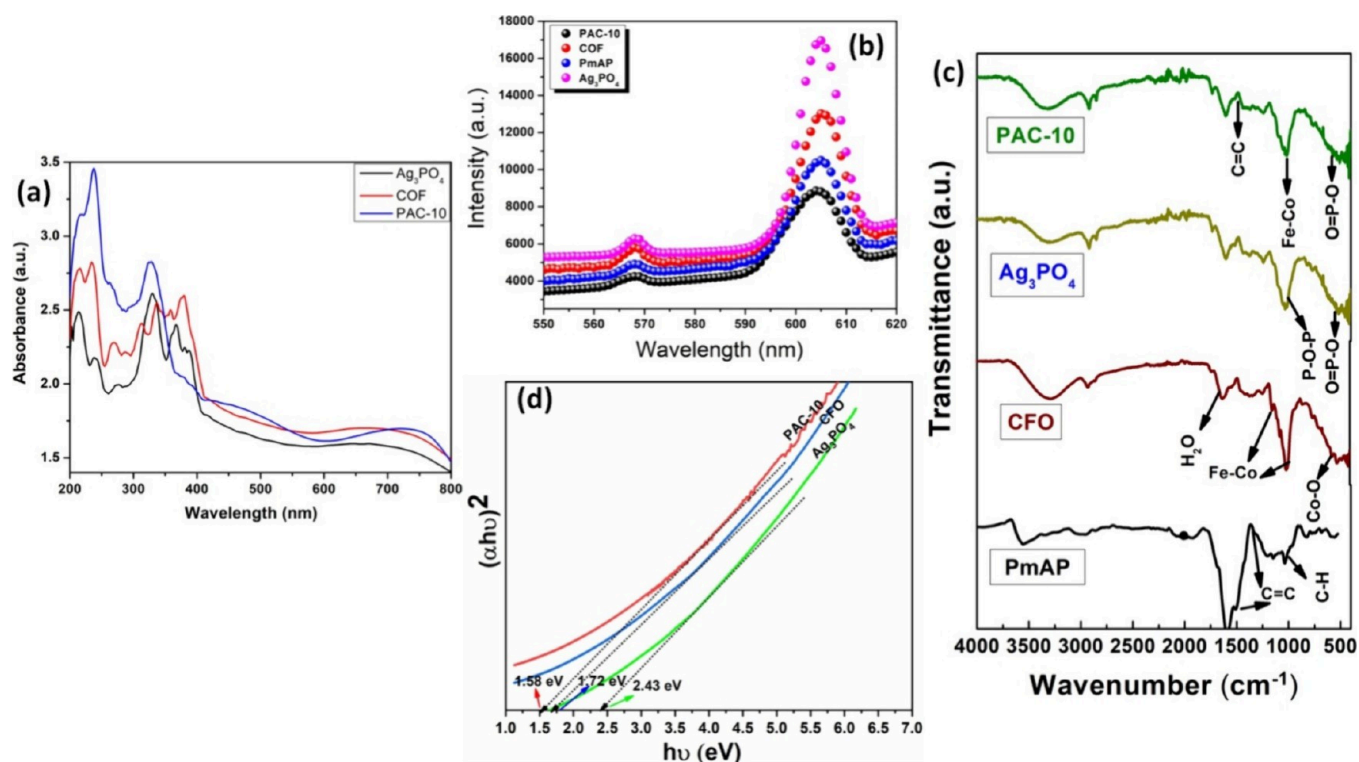
Figure 6. (a) UV−vis DRS spectra, (b) PL spectra, (c) FTIR spectra of $CoFe_2O_4$, Ag_3PO_4, and $PmAP/Ag_3PO_4/CoFe_2O_4$ composites; and (d) the plots of $(\alpha h\nu)^2$ vs $h\nu$ for $CoFe_2O_4$, Ag_3PO_4, and PAC-10 composite, respectively.

35.3°, 43.2°, 53.2°, 56.8°, and 62.5° which are characteristic of the spinel ferrite structure and matched to the (220), (311), (400), (422), (511), and (440) planes, respectively (JCPDS standard data, Card No. 22-1086).[40] The characteristic peak of PmAP is not clearly observed in PAC-10 due to its relatively lower intensity. The XRD pattern of Ag_3PO_4 corresponds to the cubic crystal form (JCPDS code no. 06-0505).[41] The diffraction pattern of the PAC-10 composite shows similar patterns of peaks including characteristic planes of Ag_3PO_4 (210), (110), (310), and (511) and CFO (220), (311), (320), (440), etc. confirming the effective combination of the CFO and Ag_3PO_4 in the composite catalyst. From the SAED array of the PAC-10, the polycrystallinity of the heterostructure nanocomposite could be recognized. The patterns of the concentric rings of the PAC-10 composite are assigned to the planes of both the semiconductors on the surface of polymeric layers.[42] This confirms the formation of the PAC-10 composite effectively on the conducting PmAP layers. The XRD analysis data were further matched with the microscopic structures of $CoFe_2O_4$ and Ag_3PO_4, inspected through HRTEM with SAED images, and depicted in Figure 4. The diffraction ring pattern shows a light-dark pattern in a ring-like arrangement. The diffraction rings are identified from inner to outer as the (210), (211), (310), (511), and (440) planes, which provide evidence of the presence of both semiconductor crystals. The SAED images of PAC-10 samples show spotty ring (discontinuous ring) patterns, revealing their crystalline spinel structure of CFO and cubic crystal structure of Ag_3PO_4. Measured interplanar spacing (d_{hkl}) from SAED patterns are in good agreement with the values in the standard data (JCPDS Card No. 22-1086). The distances between the adjacent lattice fringes were measured to be 0.29 and 0.23 nm, which corresponded to the d-spacings of the (220) of CFO and

(210) of Ag_3PO_4 nanoparticle planes, respectively, showing that the particles are deeply connected on the polymer surface. Furthermore, the investigation presented above suggests that the conductive PmAP structured layers facilitated the uniform and efficient growth of the crystals, resulting in the formation of a composite heterojunction system.

To obtain information about the elemental and oxidation states on the surface and interface, an XPS analysis of PAC-10 was carried out. As seen from Figure 5a, the full XPS spectral survey displayed all the elemental peaks present in the PAC-10 composite. No peaks for any other elements support the purity of the sample. The spectrum of individual elements was analyzed to know their chemical state. In Figure 5b, the Co 2p spectrum with two main peaks at 873.33 and 855.71 eV corresponds to binding energies of Co 2p1/2 and Co 2p3/2, respectively, which indicates Co^{2+} ion presence. The other two shoulder peaks observed are ascribed to the satellite peaks. The peaks at 711.21 and 724.62 eV in the Fe 2p spectrum (Figure 5c) refer to binding energies of Fe 2p3/2 and Fe 2p1/2, respectively, and the peak at 718.01 eV is related to the shakeup satellite peak, confirming that Fe is mainly present as Fe^{3+} state in PAC-10 composite.[43,44] The O 1s spectrum (Figure 5d) consisting of two peaks at 529.25 and 533.69 eV corresponds to lattice oxygen and the surface hydroxyl groups in the composite, respectively. The O 1s scan confirms the presence of oxygen moiety in the composite abundantly in the form of $CoFe_2O_4$, PmAP, and Ag_3PO_4. The Ag 3d spectrum of PAC-10 is displayed in Figure 5e, and the peaks at 368.5 and 374.5 eV correspond to binding energies of Ag 3d5/2 and Ag 3d3/2, respectively, proving that the main valence of a silver element is Ag^+. The absence of any characteristic peaks of Ag^0 suggests that metallic Ag has not been produced in the preparation process of the composite, which is consistent with

XRD results. The binding energy of P 2p at 134.18 eV is assigned to the PO_4^{3-} form of the P 2p scan (Figure 5f). Furthermore, the N 1s spectrum is divided into three peaks at 399.5, 402.05, and 407.28 eV, which can be assigned to −NH=, M−NH, and −N+=, respectively.[45,46] In particular, the presence of M−NH further proves that there is a chemical interaction among the PmAP π-conjugated structure, Ag_3PO_4, and $CoFe_2O_4$, which is also consistent with XRD and HRTEM results. The C 1s signal shows two major peaks at 285.5 and 289.6 eV. The lower binding energy feature is clearly related to aromatic carbons, whereas that at 289.6 eV reveals the presence of aromatic carbons bound to nitrogen or oxygen as shown in Figure 5h.[47]

Optical Analysis and Band Gap Determination. The optical absorption characteristics of the $CoFe_2O_4$, Ag_3PO_4, and PAC-10 samples were analyzed through UV−Vis DRS spectra. As observed in Figure 6a, the pristine $CoFe_2O_4$ and Ag_3PO_4 exhibit absorption bands having edges of 500 and 450 nm, respectively. After combining PmAP, Ag_3PO_4, and $CoFe_2O_4$, the final heterostructure photocatalyst exhibited improved light absorption capability along with broad absorption peaks in the entire solar light (200−800 nm) range, as compared to pure Ag_3PO_4 and $CoFe_2O_4$. Additionally, the initial absorption bands of PAC-10 composite between 238 and 389 nm correspond to the $\pi-\pi^*$ transition caused by the benzenoid ring and the conjugated polymeric chains of PmAP. The absorption bands at around 589 and 650 nm might be due to the $n-\pi^*$ transition, which corresponds to heteroatoms like nitrogen and oxygen going through nonbonding lone pair electron transitions.[48] Overall, the incorporation of PmAP in the ternary composite, $PmAP/Ag_3PO_4/CoFe_2O_4$, helps in the absorption of a wider range of visible/solar lights, which in turn improves the photocatalytic efficiency of the material.

The photoactive efficacy and the fate of the charge carriers upon illumination of photon were analyzed from the photoluminescence (PL) spectra of the synthesized materials (Figure 6b) recorded after excitation at 410 nm. The figure depicts a significant reduction of PL intensity in PAC-10 as compared to the individual components, suggesting that the e^-/h^+ separation is enhanced in the ternary composite. In other words, the recombination of charged species is lowest in the case of PAC-10 composite owing to the migration of electrons through the Z-scheme transfer path. The employment of PmAP as an electron mediator created a conducting charge-transferring channel that improved the interfacial electron migration across the Ag_3PO_4 and CFO particles, ultimately strengthening the separation efficiency of electron−hole pairs.

The FTIR spectra of different catalysts are depicted in Figure 6c. The FTIR of PmAP shows two distinct absorption bands at 1585 and 1494 cm^{-1} due to the C=C stretching vibrations of the quinoid and benzenoid rings, respectively. Stretching vibrations (C−N) of conjugated aromatic rings and stretching of the polaron (C−N−C) are responsible for the peak at about 1298 cm^{-1} and the weak shoulder at 1240 cm^{-1}, respectively. The stretching vibration of N−Q−N (where Q stands for quinoid ring) causes the strong band at 1110 cm^{-1}. The C−H bond bending vibrations are represented by the peaks at 830 and 516 cm^{-1}. The strong broadband, appearing at 594 cm^{-1}, in the FTIR spectrum of CFO, is caused by the intrinsic Co−O stretching vibration of spinel ferrite. The peaks at around 1015 and 1162 cm^{-1} can be attributed to the Fe−Co alloy system. The distinctive peaks for pure Ag_3PO_4 appeared at 1009 and 553 cm^{-1}, respectively, and they represent the bending vibrations of the −=P−O groups and the asymmetric stretching vibrations of the P−O−P groups. The entire above signature peaks of individual materials are seen in the spectrum of the PAC-10 heterojunction system signifying the successful synthesis of the hybrid catalysts with the desired structures and functional groups.

The band gap energy (E_g) of Ag_3PO_4, $CoFe_2O_4$, and PmAP/Ag_3PO_4/$CoFe_2O_4$, estimated by extending the linear portion of the $(\alpha h\nu)^n$ vs $h\nu$ plots,[43,47] are found to be 2.43, 1.72, and 1.58 eV, respectively (Figure 6d). The observed band gap values of CFO and Ag_3PO_4 are similar to the previously reported values.[43] The addition of PmAP significantly affects the band gap value of the resulting heterojunction system (PAC-10). As seen in Figure 6d, the PAC-10 composite exhibits a band gap value lowered by 0.85 units from Ag_3PO_4 and 0.14 units from CFO. The decreased band gap energy indicates improved electrical and optical properties of the hybrid material after the incorporation of PmAP acting as an electron shuttle.[49−51] It could be related to the uniform dispersion of Ag_3PO_4 and CFO particles on the PmAP sheets, as evident from the morphological analysis, which creates conductive networks throughout the matrix.[49−51] Furthermore, the decrease in the band gap value after the formation of the Z-scheme heterojunction system implies the electronic coupling between the semiconductor CFO and Ag_3PO_4, owing to the unique conducting surface of the polymer.

Electrochemical Analysis. The as-synthesized materials were first examined using Mott−Schottky (M−S) plots to identify the flat-band potentials and nature (n- or p-type) semiconducting materials. A simple M−S analysis is detailed in Figure S1a,b for CFO and PmAP (ESI). The slope of the curve indicates the semiconductor charge carrier density, whereas the intercept on the x-axis signifies the flat-band potential. From the figure, the M−S plots for both CFO and PmAP display p-type behavior. On extrapolation of positive slope to the x-axis, the estimated flat band values vs RHE are +1.1 and +1.32 V, respectively. Again, Figure S1c demonstrates the semicircular Nyquist plots of the Z-scheme PAC-10 composite. In general, a smaller arc radius indicates a reduced barrier to charge transfer, which causes electrons to migrate over the contact more quickly.[43,52] Herein, a small arc radius of the PAC-10 composite expresses swift electron migration within the heterojunction of the catalysts.

VSM and BET Surface Area Analyses. The magnetic properties of pure CFO and the PAC-10 composite were investigated with a vibrating sample magnetometer (VSM) at room temperature, and magnetization curves are presented in Figure S2 (ESI) which represents the magnetic behavior of the samples. As evident, the saturation magnetization (M_s) of CFO (42.63 emu/g) is decreased in the case of PAC-10 (29.58 emu/g) due to the addition of nonmagnetic components in the composite but is still sufficient enough for effective separation by use of an external magnet (inset Figure S2).

Furthermore, to know the effect of the PmAP on the composite, the surface area of the catalysts was analyzed and the BET results show that the specific surface area of neat CFO (25.8 m^2/g) is relatively lower than the previously reported value primarily due to higher agglomeration of nanoparticles in the present case.[53] On the addition of PmAP, the surface area is increased by about 25% (32.4 m^2/g) due to the incorporation of layered PmAP and Ag_3PO_4 nanoparticles onto CFO in the PAC-10 heterojunction system.
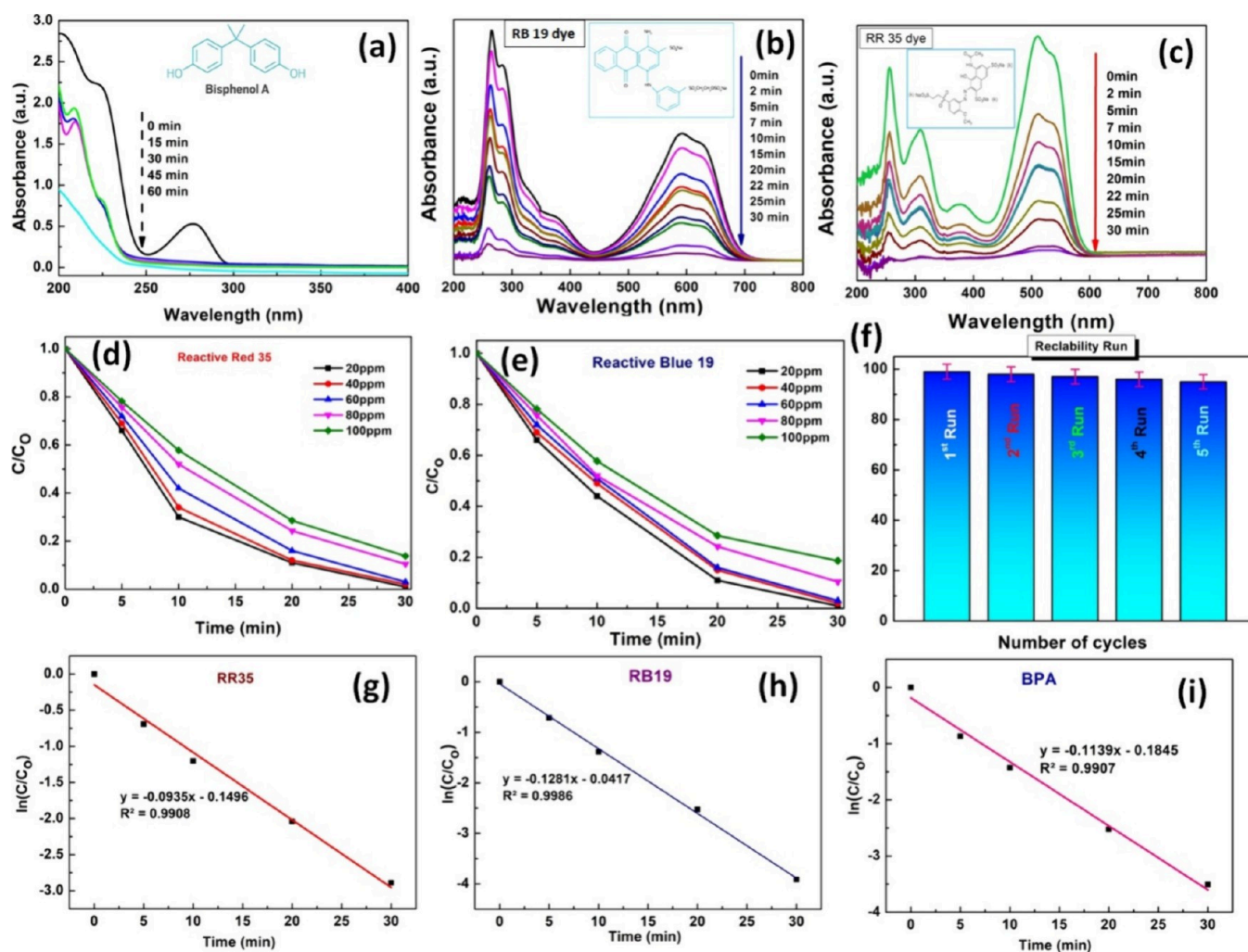
Figure 7. Photocatalytic activity of PAC-10 composites (catalyst dosage: 0.05 g) for (a) BPA (70 mg/L), (b) RB 19, and (c) RR 35 (100 mg/L) pollutants degradation under visible light irradiation. (d, e) Photocatalytic activity of the PAC-10 composite with different initial reactive dye concentrations, (f) Recyclability tests up to 5th run over the PAC-10 catalyst with RB 19 dye (catalyst, 0.05 g; concentration, 100 mg/L). (g–i) Linear fitting of the visible light degradation profiles to the first-order kinetic model of RR 35 (20 mg/L), RB 19 (20 mg/L), and BPA (20 mg/L) in the presence of the PAC-10 catalyst.

High Concentrated Contaminant Removal Analysis. The photoactivity of the as-synthesized Ag$_3$PO$_4$, CFO, PmAP, and PAC-10 was investigated by taking 100 mg/L reactive dyes (RB 19, RR 35) and 70 mg/L of BPA solutions. A comparative study of the ability to degrade the highly concentrated colored/colorless organics with and without light irradiation is illustrated in Figure S3 (ESI). All dark and visible light reactions were consistently performed under identical conditions to assess the adsorption and degradation capabilities of the studied samples. The percentage of RB-19 adsorption by PmAP, CFO, Ag$_3$PO$_4$, and PAC-10, are found to be 22.3, 13.5, 8.5, and 28.4%, respectively. This adsorptive ability of PmAP is primarily due to the strong lone pair electrons present in −NH$_2$/OH functional groups that provide efficient adsorption ability. CFO exhibits good adsorption to contaminants owing to the positively charged surface of the catalyst. In comparison, PAC-10 exhibits greater adsorption ability for both BPA and reactive dyes than the individual catalysts. Concurrently, the visible light adsorption/degradation of RB 19 yielded 33.7, 32.4, 90.3, and 99%, respectively demonstrating the effectiveness of the samples in degrading the dye under visible light irradiation. Similarly, RR 35 adsorption under dark conditions

shows the removal of 23.4, 13.5, 8.5, and 28.4% in the presence of PmAP, CFO, Ag$_3$PO$_4$, and PAC-10, respectively. Notably, visible light reactions of PmAP, CFO, Ag$_3$PO$_4$, and PAC-10 resulted in adsorption/degradation of 33.5, 35.5, 92, and 99.3%, respectively. In the case of BPA, the percentages of adsorption using PmAP, CFO, Ag$_3$PO$_4$, and PAC-10 are 28.3, 10.5, 15.4, and 20.4%, respectively, whereas visible light adsorption/degradation results are 36.4, 25.2, 64, and 99%, respectively.

The details of photoactivity of PAC-10 toward varying concentrations of BPA, RB 19, and RR 35 under visible light illumination are summarized in Figure 7. After agitation of BPA/dye solution with a catalyst for 30 min in the dark, the reactant solution was irradiated with visible light. Figure 7a–c exhibits repetitive UV−visible spectral scans of reactive dyes (100 mg/L) and BPA (70 mg/L) over the reaction period. It is seen that almost 100% of BPA is degraded within 60 min while complete degradation of reactive dyes is archived in about 30 min of irradiation. The fast degradation of highly concentrated reactive dyes/BPA using a small amount (0.33 g/L) of PAC-10 is worth noting. It may be noted that there is no shift in the absorbance band in the degradation process of reactive dyes or
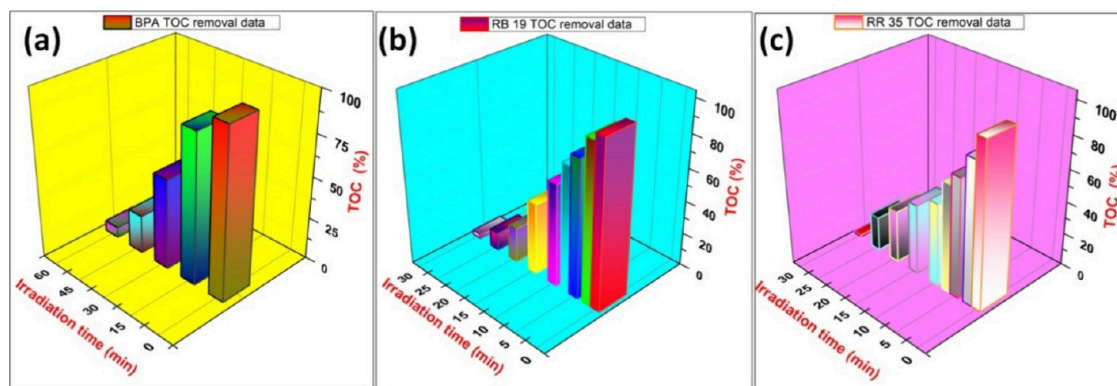
Figure 8. TOC of the irradiated (a) BPA, (b) RB 19, and (c) RR 35 using the PAC-10 heterojunction.

BPA, indicating their mineralization to smaller products like CO_2 and H_2O rather than fragmentation of organics into their smaller organic byproducts.[52] The recyclability test for five consecutive cycles using RB 19 dye (100 mg/L) shows a marginal decrease in activity indicating the stability and efficiency of PAC-10. The experimental degradation data were well-fitted to the first-order kinetic model (eq 1) with high correlation coefficient (R^2) values.

$$\ln {C_0}/{C} = Kt \tag{1}$$

where C and C_0 are the final and initial concentrations of dyes/BPA degraded at time t, respectively, and k is the observed rate constant (time^{-1}). The results were treated as first-order kinetics by plotting $\ln(C_0/C)$ versus t.

Since durability represents an essential feature of a viable photocatalyst, comparative recycling studies using RR 35 were also carried out in the presence of pure CFO, Ag_3PO_4, and PAC-10 composite under identical conditions, and results are presented in Figure S3g. In comparison, the PAC-10 showed a significantly higher reusability feature than individual catalysts. Pure Ag_3PO_4 is found to have a high rate of surface corrosion,[54,55] which degraded 60−80% of RB-19 and RR 35 dyes (100 ppm) and has essentially little capacity for recycling. Many researchers tried to prevent the self-corrosion property of Ag_3PO_4 with surface modifications and doping such as Zr doping, La, Zr codoped, and facet engineering of Ag_3PO_4.[54,55] This work successfully demonstrated the prevention of corrosion of Ag_3PO_4 structure in PAC-10 heterojunction with increased recycling ability of the catalyst. To confirm the intactness of the sample, the filtrates were collected after the fourth cycle of the photoreaction and analyzed through the ICP-OES method to detect the amount of leached metallic ions from the PAC-10 catalyst. Interestingly, no metallic ions are detected in the filtrate, indicating that the Z-scheme catalyst is stable, recyclable, and effective for the photo-degradation of organic contaminants.

Mineralization Study through TOC Analysis. Total organic carbon (TOC) analyses at different time intervals during the photodegradation of BPA, RB 19, and RR 35 under optimized conditions were performed to monitor the loss of organic carbon due to mineralization (Figure 8a−c). From the figure, it is evident that the TOC removal due to photo-mineralization of BPA, RB-19, and RR-35 is 93.7, 97.1, and 97.7%, respectively. It is worth noting that for a particular dye or BPA, the degradation efficiency (%) is higher than the percentage of TOC removed under the same testing

conditions, presumably due to the absorption of some free radicals by the pollutants along with other products emerging from degradation. From the above observations, it can be concluded that almost complete removal of these organic pollutants can be achieved from synthetic wastewater using PAC-10 under visible light irradiation. Moreover, the reactant solutions became practically colorless after the photocatalytic treatment.

Mechanistic Analysis. Through the PAC-10 catalyst, we have concluded swift mineralization of highly concentrated organic molecules. Pristine Ag_3PO_4 and CFO did not show much efficacy in activity and recyclability in high-concentration dye removal experiments, while PAC-10 showed almost quadrupled activity with good stability compared to the individual catalysts presumably due to maneuvering of the Z-scheme transfer path of photogenerated electrons and holes rather than conventional heterostructures. Furthermore, the conducting PmAP polymer has intriguing characteristics that make it a viable option to be used as a solid-state electron mediator in the Z-scheme design. The amino and other functional groups present in PmAP may favor its binding with other substances perfectly and as such, the PmAP-based composites will have more active sites for greater capability of interaction with the contaminants for the reaction. Owing to the special π-conjugated frameworks, PmAP has excellent environmental stability, higher electrical and proton trans-mission in acidic environments, as well as unique redox properties.[56] In addition, the PmAP has a thin π-conjugated structure with a relatively higher surface area that can provide better support to develop a solid interaction between the semiconductor materials.[57] From the above discussion, it may be concluded that the PmAP having a π-conjugated structure, unique electrochemical properties, the presence of distinctive functional groups, and conductive nature helps in the proper electron transfer mechanism in the Z-scheme heterojunction system.

The process of photocatalysis for the removal of pollutants involves the initial excitation of electrons from the valence band (VB) to the conduction band (CB) by using photons with enough energy. The availability and separation of electron and hole pairs are the cornerstones of this procedure. Generally, superoxide ($\cdot O_2^-$) and hydroxyl ($\cdot OH$) radicals are produced on the semiconductor surface having appropriate band edge alignments. Both reactive species can break down the organic contaminants into less harmful compounds like H_2O, CO_2, etc. Superoxide anion radical formation requires the CB to be higher (more −ve) than the oxygen-reducing

potential (-0.33 V) while hydroxyl radical generation requires the VB to be lower (more +ve) than the potential for water oxidation (2.33 V).[58,59] In the case of the CFO semiconductor, the formation of hydroxyl radicals is less likely as its VB position lies above the potential of water oxidation (+2.17 V). On the other hand, the Ag_3PO_4 has a deep VB that can easily produce hydroxyl radicals but not superoxide radicals owing to the positive CB position (+0.45 V). Due to the lack of potency of the individual catalyst band structure, the type-II charge transfer pathway is not possible to produce the desired radicals. Hence, a tenable mechanism is constructed for the PAC-10 photocatalytic behavior through the Z-scheme charge transfer pathway and explained further.[14]

A feasible mechanism for the action of PmAP as a solid-state electron mediator in the present photocatalytic system using the Z-scheme is depicted in Figure 9. As shown in the figure,
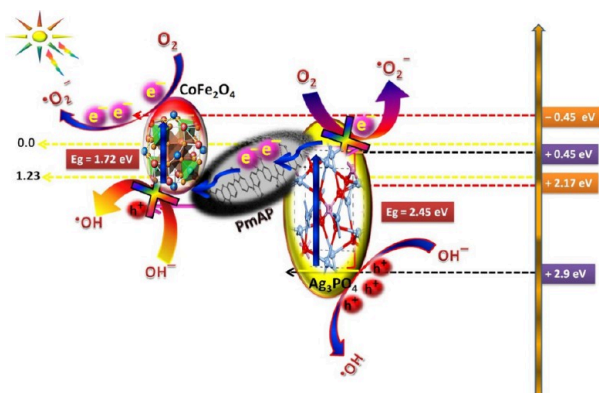

Figure 9. Mechanism of photoactivity in a Z-scheme photocatalysis system consisting of $CoFe_2O_4/PmAP/Ag_3PO_4$ under visible-light irradiation.

Ag_3PO_4 (O_2 photocatalyst) and CFO (H_2 photocatalyst) adhered to one another on the surface of the PmAP conducting polymer. Electrons in the VB of Ag_3PO_4 and the CFO are photoexcited to move into the CB with exposure to visible light. The lack of an absorption edge for PmAP suggests that the PmAP in the current system does not have an energy gap, based on the UV−vis spectra[10,42] of PmAP/CFO (Figure

S4). These facts suggest that PmAP does not participate in the production of electrons and holes through the absorption of visible light. Alternatively, PmAP used in this study exhibits the characteristics of an electron conductor. Hence the photo-generated electrons available in the CB of Ag_3PO_4 quickly get transferred to the VB of CFO since the CFO and Ag_3PO_4 particles are strongly connected with the conductive PmAP layer. A full cycle for removing organic pollutants is achieved when the holes in the VB of Ag_3PO_4 oxidize water to ·OH and the electrons in the CB of CFO reduce O_2 to $·O_2^-$ simultaneously. Previous findings[14,61] reported this direction of electron flow efficiently. In this work, the PmAP conducting polymer creates paths that allow electrons created in the O_2-developing photocatalyst to travel to the H_2-developing photocatalyst, which, in turn, uses the Z-scheme pathway for the destruction of organics. Unlike the type-II system, which drives the flow of electrons from the upper CB to the lower CB, in the current Z-scheme system, the electrons flow from the CB of Ag_3PO_4 to recombine with the VB of CFO through the conducting PmAP and produce the desired active species for the reactions. For this, a quenching study and terephthalic probing experiment were conducted to determine the sorts of free radicals developed during the photoreaction to verify the Z-scheme mechanism was explained henceforth.

Verification of the Z-Scheme Charge Transfer Pathway. To gain information on the Z-scheme charge transfer pathway, the terephthalic acid fluorescence probe technique was used, to trap the ·OH radical formation upon illumination of light energy.[60,61] Terephthalic acid is one of the most appropriate ·OH probe compounds for the elucidation of the photocatalytic catalytic mechanism. This acid reacts to ·OH, present in the environment, to form a highly fluorescent product viz. 2-hydroxy terephthalic acid that shows an emission at 426 nm. For this, 0.05 g of PAC-10, Ag_3PO_4, $CoFe_2O_4$, and PmAP catalysts were added to a terephthalic acid solution. After the solution was exposed to light, the fluorescence of the clear supernatant was measured. Figure 10a illustrates a noticeable increase in the PL spectral intensity for the heterostructure and Ag_3PO_4. Hence it validates that a larger quantity of ·OH is forming on the PAC-10 photocatalyst hybrid surface, which was mostly dependent on Z-scheme transfer pathways. Interestingly, Ag_3PO_4 is showing a good
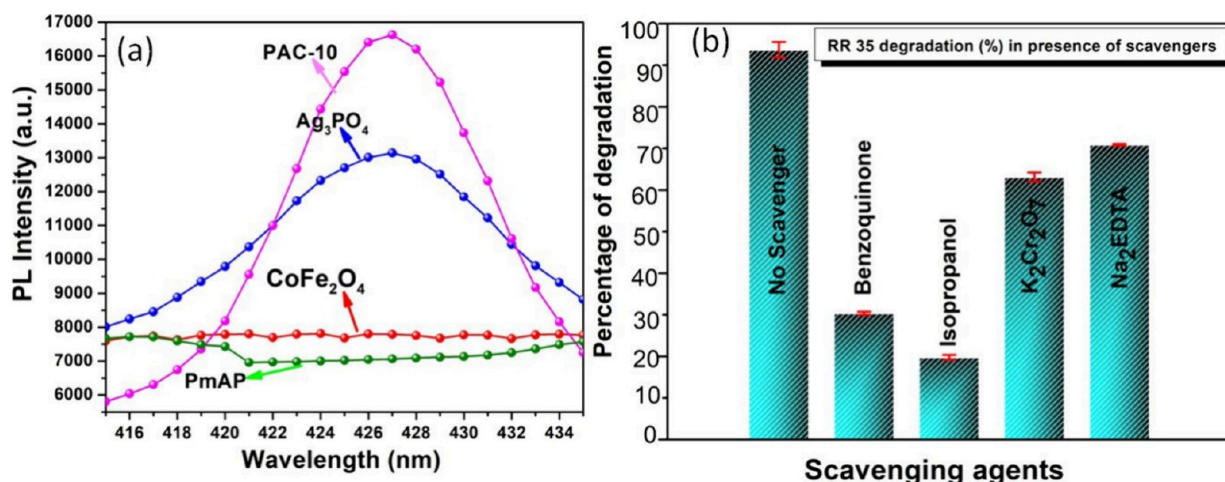

Figure 10. (a) Fluorescence spectra analyzed with 4×10^{-3} M NaOH solution of terephthalic acid (excitation at 315 nm) in the presence of catalysts. (b) Effect of scavenging agents presence during 120 mg/L of RR 35 dye degradation.

amount of ·OH formation, due to its deeper VB position. In contrast, no fluorescent peak at 426 nm is observed in the cases of pristine CFO and PmAP implying no ·OH radical formation on the surface of the PmAP and CFO. To further appraise the participating active species in the photodegradation of a reactive dye (RR 35) with the exposure of light, different quenchers were added to a solution containing RR 35 (120 mg/L) and PAC-10 catalyst (0.05 g). From the analysis of the degradation of dye in the presence of different quenchers, a drastic reduction in the photodegradation percentage is observed in the cases of benzoquinone and 2-propanol (Figure 10b). This further indicates the greater contribution of ·OH and ·O_{2-} radicals in the degradation of the organics. Also, some percentage of degradation was decreased in the presence of e^- and h^+ scavengers such as $K_2Cr_2O_7$ and Na_2EDTA, respectively, indicating their contribution to a lesser extent in the degradation process. From the above, it is clear that superoxide and hydroxyl radicals are primarily responsible for the photodegradation process of PAC-10.

Furthermore, to authenticate the Z-scheme transfer pathway of PAC-10, an in situ reduction of platinum (Pt^{4+}) to Pt^0 experiment was performed on the surface of the catalyst. For this, photo deposition of platinum using stoichiometric $H_2PtCl_6\cdot6H_2O$ (1.0 wt % of PAC-10) over PAC-10 was observed in the presence of visible light. Before the experiment, the catalyst suspension was purged with N_2 and then treated with light illumination for 30 min. The catalyst sample, collected after proper washing with distilled water until the removal of chloride, was dried at 70 °C. The dried sample was tested under HRTEM analysis to verify the metallic Pt deposition area. In the HRTEM image of Pt-PAC-10 (Figure S5, ESI), the estimated d-spacing is found to be 0.22, which is indexed to the (111) reflection of face-centered cubic atomic planes of the Pt particles on the CFO particles and nearby its surface. This further confirms that the deposition of Pt^0 takes place on the surface of CFO rather than other surfaces. In addition, there is no overlapping of lattice fringes of Pt^0 and Ag_3PO_4, which further supports that platinum was reduced mostly on the surface of the CFO, and there may be some on PmAP (during the e-shuttle process). This experiment confirms that the transfer of charge carriers through the Z-scheme pathway and the electrons are available on the surface of CFO.[61]

CONCLUSIONS

In summary, we have shown that PmAP, which is readily synthesized, may be utilized in a Z-scheme photocatalytic setup as a solid-state electron mediator. PmAP, in contrast to other conducting polymers, effectively transfers photoexcited electrons from the positive conduction band containing photocatalyst to the negative conduction band containing photocatalyst, thereby greatly enhancing the activity with a higher redox ability. Finding a balance between the particle morphologies on the PmAP layers is crucial for effective electron transport in a Z-scheme system. The current work has opened up new avenues for the efficient and innovative construction of highly concentrated organic contaminants mineralization photo systems by using the polyaniline derivative.

ASSOCIATED CONTENT

ⓢ Supporting Information

The Supporting Information is available free of charge at https://pubs.acs.org/doi/10.1021/acsomega.3c09943.

Characterization; experimental sections; electrochemical analysis; VSM analysis; and other figures (PDF)

AUTHOR INFORMATION

Corresponding Authors

Alaka Samal − Department of Chemistry, Utkal University, Vani Vihar, Odisha 751004, India; ● orcid.org/0000-0002-4089-8463; Email: samal.alaka@gmail.com

Nigamananda Das − Department of Chemistry, Utkal University, Vani Vihar, Odisha 751004, India; ● orcid.org/0000-0002-8281-8345; Email: dasn.chem@utkaluniversity.ac.in

Authors

Chirasmayee Mohanty − Department of Chemistry, Utkal University, Vani Vihar, Odisha 751004, India

Ajaya K. Behera − Department of Chemistry, Utkal University, Vani Vihar, Odisha 751004, India

Complete contact information is available at:
https://pubs.acs.org/10.1021/acsomega.3c09943

Notes

The authors declare no competing financial interest.
Ethics approval not applicable: this manuscript does not involve research on humans or animals. Consent to participate and publish: all authors consented to participate in drafting and publishing this manuscript.

REFERENCES

(1) Gao, H.; Yang, B. J.; Li, N.; Feng, L. M.; Shi, X. Y.; Zhao, W. H.; Liu, S. J. Bisphenol A and Hormone-Associated Cancers. Medicine 2015, 94 (1), No. e211.

(2) Brede, C.; Fjeldal, P.; Skjevrak, I.; et al. Increased migration levels of bisphenol A from polycarbonate baby bottles after dishwashing, boiling and brushing. Food Addit Contam. 2003, 20, 684−689.

(3) Howdeshell, K. L.; Peterman, P. H.; Judy, B. M.; et al. Bisphenol A is released from used polycarbonate animal cages into water at room temperature. Environ. Health Perspect. 2003, 111, 1180−1187.

(4) Gouvea, C. A.; Wypych, F.; Moraes, S. G.; Duran, N.; Nagata, N.; Peralta-Zamora, P. Semiconductor-assisted photocatalytic degradation of reactive dyes in aqueous solution. Chemosphere 2000, 40 (4), 433−440.

(5) Mohan, H.; Vadivel, S.; Lee, S. W.; Lim, J. M.; Lovanh, N.; Park, Y. J.; Shin, T.; Seralathan, K. K.; Oh, B. T. Improved visible-light-driven photocatalytic removal of Bisphenol A using V2O5/WO3 decorated over Zeolite: Degradation mechanism and toxicity. Environmental Research 2022, 212, No. 113136.

(6) Garg, A.; Singhania, T.; Singh, A.; et al. Photocatalytic Degradation of Bisphenol-A using N, Co Codoped TiO2 Catalyst under Solar Light. Sci. Rep 2019, 9, 765.

(7) Yuan, Z.; Huang, H.; Li, N.; Chen, D.; Xu, Q.; Li, H.; He, J.; Lu, J. All-solid-state WO3/TQDs/In2S3 Z-scheme heterojunctions bridged by Ti3C2 quantum dots for efficient removal of hexavalent chromium and bisphenol A. *Journal of Hazardous Materials* 2021, 409, No. 125027.

(8) Zhang, R.; Yu, J.; Zhang, T.; Zhao, C.; Han, Q.; Li, Y.; Liu, Y.; Zeng, K.; Cai, L.; Yang, Z.; Ma, Y. A novel snowflake dual Z-scheme Cu2S/RGO/Bi2WO6 photocatalyst for the degradation of bisphenol A under visible light and its effect on crop growth. *Colloids Surf., A* 2022, 641, No. 128526.

(9) Athar, M. S.; Rasool, Z.; Muneer, M.; Altass, H. M.; Althagafi, I. I.; Ahmed, S. A. Fabrication of Direct Z-Scheme CoNiWO4/Ph-gC3N4 Heterocomposites: Enhanced Photodegradation of Bisphenol A and Anticancer Activity. *ACS Omega* 2023, 8 (41), 38272−38287.

(10) Kudo, A.; Miseki, Y. Heterogeneous photocatalyst materials for water splitting. *Chem. Soc. Rev.* 2009, 38 (1), 253−278.

(11) Tada, H.; Mitsui, T.; Kiyonaga, T.; Akita, T.; Tanaka, K. All-solid-state Z-scheme in CdS−Au−TiO$_2$ three-component nano-junction system. *Nat. Mater.* 2006, 5, 782−786.

(12) Gopalasamy, T.; Gopalswamy, M.; Gopichand, M.; Raj, J. January 19). Poly Meta-Aminophenol: Chemical Synthesis, Characterization and Ac Impedance Study. *Journal of Polymers* 2014, 2014, 1−11.

(13) Bubu, Y.; Chen, Z. Role of Polyaniline on the Photocatalytic Degradation and Stability Performance of the Polyaniline/Silver/Silver Phosphate Composite under Visible Light. *ACS Appl. Mater. Interfaces* 2014, 6 (20), 17589−17598.

(14) Iwase, A.; Ng, Y. H.; Ishiguro, Y.; Kudo, A.; Amal, R. Reduced Graphene Oxide as a Solid-State Electron Mediator in Z-Scheme Photocatalytic Water Splitting under Visible Light. *J. Am. Chem. Soc.* 2011, 133 (29), 11054−11057.

(15) Yadav, A.; Kumar, H.; Sharma, R.; Kumari, R. Influence of polyaniline on the photocatalytic properties of metal nanocomposites: A review. *Colloid and Interface Science Communications* 2021, 40, No. 100339.

(16) Shirota, Y.; Kageyama, H. Charge Carrier Transporting Molecular Materials and Their Applications in Devices. *Chem. Rev.* 2007, 107, 953−1010.

(17) Shang, M.; Wang, W.; Sun, S.; Ren, J.; Zhou, L.; Zhang, L. Download Citations Efficient Visible Light-Induced Photocatalytic Degradation of Contaminant by Spindle-like PANI/BiVO4. *J. Phys. Chem. C* 2009, 113, 20228−20233.

(18) Zhang, H.; Zong, R.; Zhao, J.; Zhu, Y. Dramatic Visible Photocatalytic Degradation Performances due to Synergetic Effect of TiO2 with PANI. *Environ. Sci. Technol.* 2008, 42, 3803−3807.

(19) Huang, H.; Liu, Y.; Lee, S.; Kang, Z. Polymer (Polyanilines) Nanoparticles: A Superior Catalyst for Hydrocarbon Selective Oxidation. *J. Mater. Chem.* 2012, 22, 337−340.

(20) Sonu, D. V.; Sharma, S.; Raizada, P.; Hosseini-Bandegharaei, A.; Kumar Gupta, V.; Singh, P. Review on augmentation in photocatalytic activity of CoFe$_2$O$_4$ via heterojunction formation for photocatalysis of organic pollutants in water. *J. Saudi Chem. Soc.* 2019, 23 (8), 1119−1136.

(21) Benlembarek, M.; Salhi, N.; Benrabaa, R.; Djaballah, A.; Boulahouache, A.; Trari, M. Synthesis, physical and electrochemical properties of the spinel CoFe$_2$O$_4$: Application to the photocatalytic hydrogen production. *Int. J. Hydrogen Energy* 2022, 47 (15), 9239−9247.

(22) Kamilla, S.; Kumar, A. Cobalt ferrite: A review. *Materials Today: Proceedings* 2023, 81, 508−510.

(23) Abbas, N.; Rubab, N.; Sadiq, N.; Manzoor, S.; Khan, M. I.; Fernandez Garcia, J.; Barbosa Aragao, I. B.; Tariq, M.; Akhtar, Z.; Yasmin, G. Aluminum-Doped cobalt ferrite as an efficient photocatalyst for the abatement of methylene blue. *Water* 2020, 12, 2285.

(24) Renukadevi, S.; Jeyakumari, A. P. A one-pot microwave irradiation route to synthesis of CoFe2O4-g-C3N4 heterojunction catalysts for high visible light photocatalytic activity: exploration of efficiency and stability. *Diam. Relat. Mater.* 2020, 109, No. 108012.

(25) Sebai, I.; Salhi, N.; Rekhila, G.; Trari, M. Visible light induced H2 evolution on the spinel NiAl2O4 prepared by nitrate route. *Int. J. Hydrogen Energy* 2017, 42, 26652−26658.

(26) Li, C.; Che, H.; Huo, P.; Yan, Y.; Liu, C.; Dong, H. Confinement of ultrasmall CoFe2O4 nanoparticles in hierarchical ZnIn2S4 microspheres with enhanced interfacial charge separation for photocatalytic H2 evolution. *J. Colloid Interface Sci.* 2021, 581, 764−773.

(27) Bagtache, R.; Sebai, I.; Trari, M. Visible light induced H2 evolution on the hetero-junction Pt/CuCo2O4 prepared by hydro-thermal route. *Sol. Energy* 2020, 211, 971−976.

(28) Amirulsyafiee, A.; Khan, M. M.; Harunsani, M. H. Ag3PO4 and Ag3PO4−based visible light active photocatalysts: Recent progress, synthesis, and photocatalytic applications. *Catal. Commun.* 2022, 172, No. 106556.

(29) Xiang, Q. J.; Yu, J. G.; Jaroniec, M. Preparation and Enhanced Visible-Light Photocatalytic H2-Production Activity of Graphene/C3N4 Composites. *J. Phys. Chem. C* 2011, 115, 7355−7363.

(30) Yi, Z.; Ye, J.; Kikugawa, N.; Kako, T.; Ouyang, S.; Stuart Williams, H.; Yang, H.; Cao, J.; Luo, W.; Li, Z.; Liu, Y.; Withers, R. L. *Nat. Mater.* 2010, 9, 559−564.

(31) Ye, H.; Xia, L.; Wang, Y.; et al. Magnetic Ag3PO4/CoFe2O4 Z-scheme heterojunction material for photocatalytic decomposition of ofloxacin. *J. Mater. Sci: Mater. Electron* 2023, 34, 2090.

(32) Gebreslassie, G.; Gebrezgiabher, M.; Lin, B.; Thomas, M.; Linert, W. Direct Z-Scheme CoFe2O4-Loaded g-C3N4 Photocatalyst with High Degradation Efficiency of Methylene Blue under Visible-Light Irradiation. *Inorganics.* 2023, 11 (3), 119.

(33) Liu, Y.; Lin, Y.; Liu, Z.; Tang, J.; Chen, L.; Liu, X.; Tian, Y.; Fang, D.; Wang, J. Self-generating CoFe2O4 as electric channel in Z-scheme CoO(111)/CoFe2O4/Fe2O3 photocatalyst for synchronous photocatalytic degradation and hydrogen production. *Materials Science in Semiconductor Processing* 2022, 140, No. 106382.

(34) Ferdosi, E.; Bahiraei, H.; Ghanbari, D. Investigation the photocatalytic activity of CoFe2O4/ZnO and CoFe2O4/ZnO/Ag nanocomposites for purification of dye pollutants Sep. *Purif. Technol.* 2019, 211, 35.

(35) Wilson, A.; Mishra, S. R.; Gupta, R.; Ghosh, K. Preparation and photocatalytic properties of hybrid core−shell reusable CoFe$_2$O$_4$−ZnO nanospheres. *J. Magn. Magn. Mater.* 2012, 324, 2597−2601.

(36) Mohanty, C.; Das, N.; Behera, A. K.; Tripathy, B. C. Efficiency of Poly (m-Aminophenol) as a Novel Adsorbent for Individual/Simultaneous Removal of Organic Dyes and Hexavalent Chromium from Water Sources. *Water, Air, Soil Pollut.* 2023, 234 (3), 204.

(37) Behera, A. K.; Adhikari, B.; Kar, P. Synthesis of processable conducting poly (m-aminophenol) having structure like keto derivative of polyaniline. *Polymer Science Series B* 2015, 57, 159−166.

(38) Nishad, K. K.; Tiwari, N.; Pandey, R. K. Synthesis and characterization of ferromagnetic Fe3O4−ZnO hybrid core−shell nanoparticles. *J. Electron. Mater.* 2018, 47, 3440−3450.

(39) Liu, L.; Ding, L.; Liu, Y.; An, W.; Lin, S.; Liang, Y.; Cui, W. A stable Ag3PO4@PANI core@shell hybrid: Enrichment photocatalytic degradation with π-π conjugation. *Applied Catalysis B: Environmental* 2017, 201, 92−104.

(40) Suharyadi, E.; Muzakki, A.; Nofrianti, A.; Istiqomah, N. I.; Kato, T.; Iwata, S. Photocatalytic activity of magnetic core-shell CoFe2O4@ZnO nanoparticles for purification of methylene blue. *Materials Research Express* 2020, 7 (8), No. 085013.

(41) Kausor, M. A.; Chakrabortty, D. Optimization of system parameters and kinetic study of photocatalytic degradation of toxic acid blue 25 dye by Ag3PO4@RGO nanocomposite. *J. Nanopart. Res.* 2020, 22 (4), 93.

(42) Guo, N.; Li, H.; Xu, X.; Yu, H. Hierarchical Fe3O4@MoS2/Ag3PO4 magnetic nanocomposites: enhanced and stable photo-catalytic performance for water purification under visible light irradiation. *Appl. Surf. Sci.* 2016, 389, 227−239.

(43) Chen, Y.; Zhu, P.; Duan, M.; Li, J.; Ren, Z.; Wang, P. August). Fabrication of a magnetically separable and dual Z-scheme PANI/Ag3PO4/NiFe2O4 composite with enhanced visible-light photo-

catalytic activity for organic pollutant elimination. *Appl. Surf. Sci.* **2019**, *486*, 198−211.

(44) Wang, C.; Wang, L.; Jin, J.; Liu, J.; Li, Y.; Wu, M.; Chen, L.; Wang, B.; Yang, X.; Su, B. Probing effective photocorrosion inhibition and highly improved photocatalytic hydrogen production on monodisperse PANI@CdS core-shell nanospheres. *Appl. Catal., B* **2016**, *188*, 351−359.

(45) Zhou, T.; Zhao, Y.; Han, W.; Xie, H.; Li, C.; Yuan, M. Enhanced solvent-free selective oxidation of cyclohexene to 1,2-cyclohexanediol by polyaniline @halloysite nanotubes. *J. Mater. Chem. A* **2017**, *5*, 18230−18241.

(46) Cotarelo, M. A.; Huerta, F.; Quijada, C.; Mallavia, R.; Vázquez, J. L. Synthesis and characterization of electroactive films deposited from aniline dimmers. *J. Electrochem. Soc.* **2006**, *153*, D114.

(47) Tian, L.; Yang, X.; Cui, X.; Liu, Q.; Tang, H. Fabrication of dual direct Z-scheme g-C3N4/MoS2/Ag3PO4 photocatalyst and its oxygen evolution performance. *Appl. Surf. Sci.* **2019**, *463*, 9−17.

(48) Kaya, S.; Akyüz, B.; Özel, A. Synthesis, characterization, photophysical and surface properties of poly(amino naphthalene) and its poly(azomethine) compound. *J. Appl. Polym. Sci.* **2023**, *140* (27), No. e54021.

(49) Abdullah, O. G.; Aziz, S. B.; Saber, D. R. Characterizations of pure and Pb^{2+} ion doped methylcellulose based biopolymer electrolyte films: optical and electrical properties. *Int. J. Electrochem Sci.* **2018**, *13*, 11931−11952.

(50) Radwan, R. Electron induced modifications in the optical properties of polypropylene. *J. Phys. D Appl. Phys.* **2007**, *40*, 374.

(51) Abdullah, O. G.; Aziz, S. B.; Rasheed, M. A. Structural and optical characterization of PVA: KMnO4 based solid polymer electrolyte. *Results Phys.* **2016**, *6*, 1103−1108.

(52) Zhang, W.; Li, G.; Wang, W.; Qin, Y.; An, T.; Xiao, X.; Choi, W. Enhanced photocatalytic mechanism of Ag_3PO_4 nano-sheets using MS_2 (M = Mo, W)/rGO hybrids as co-catalysts for 4-nitrophenol degradation in water. *Appl. Catal., B* **2018**, *232*, 11−18.

(53) Behura, R.; Sakthivel, R.; Das, N. Synthesis of cobalt ferrite nanoparticles from waste iron ore tailings and spent lithium ion batteries for photo/sono-catalytic degradation of Congo red. *Powder Technol.* **2021**, *386*, 519−527.

(54) Amirulsyafiee, A.; Khan, M. M.; Khan, A.; Khan, M. Y.; Harunsani, M. H. Influence of Zr doping on Ag_3PO_4 for photo-catalytic degradation of dyes and Cr(VI) reduction under visible light irradiation. *Mater. Chem. Phys.* **2022**, *291*, No. 126673.

(55) Amirulsyafiee, A.; Khan, M. M.; Khan, M. Y.; Khan, A.; Harunsani, M. H. La, Zr co-doped Ag_3PO_4 for enhanced visible-light photocatalytic degradation of dyes and Cr(VI) photoreduction. *Chemical Physics Impact* **2022**, *5*, No. 100102.

(56) Gopalasamy, T.; Gopalswamy, M.; Gopichand, M.; Raj, J. Poly Meta-Aminophenol: Chemical Synthesis, Characterization and Ac Impedance Study. *Journal of Polymers* **2014**, *2014*, 1−11.

(57) Chen, S.; Wei, Z.; Qi, X.; Dong, L.; Guo, Y. G.; Wan, L.; Shao, Z.; Li, L. Nanostructured Polyaniline-Decorated Pt/C@PANI Core−Shell Catalyst with Enhanced Durability and Activity. *J. Am. Chem. Soc.* **2012**, *134* (32), 13252−13255.

(58) Eskandari, N.; Nabiyouni, G.; Masoumi, S.; Ghanbari, D. Preparation of a new magnetic and photo-catalyst CoFe2O4−SrTiO3 perovskite nanocomposite for photo-degradation of toxic dyes under short time visible irradiation. *Composites Part B: Engineering* **2019**, *176*, No. 107343.

(59) Askarniya, Z.; Baradaran, S.; Sonawane, S. H.; Boczkaj, G. A comparative study on the decolorization of Tartrazine, Ponceau 4R, and Coomassie Brilliant Blue using persulfate and hydrogen peroxide based Advanced Oxidation Processes combined with Hydrodynamic Cavitation. *Chemical Engineering and Processing - Process Intensification* **2022**, *181*, 109160.

(60) Dong, Y.; Feng, C.; Zhang, J.; Jiang, P.; Wang, G.; Wu, X.; Miao, H. A New p-Metal-n Structure AgBr-Ag-BiOBr with Superior Visible-Light-Responsive Catalytic Performance. *Chem. − Asian J.* **2015**, *10* (3), 687−693.

(61) Samal, A.; Das, D. P.; Nanda, K. K.; Mishra, B. K.; Das, J.; Dash, A. Reduced Graphene Oxide−Ag3PO4 Heterostructure: A Direct Z-Scheme Photocatalyst for Augmented Photoreactivity and Stability. *Chem. − Asian J.* **2016**, *11* (4), 584−595.